# Phase aberration correction for focused ultrasound transmission by refraction compensation

Mozaffarzadeh, Moein; Minonzio, Claudio; Verweij, Martin; Hemm, Simone; Daeichin, Verya

**DOI**
10.7567/1347-4065/ab19aa

**Publication date**
2019

**Document Version**
Final published version

**Published in**
IEEE International Ultrasonics Symposium 2019

Japanese Journal of Applied Physics



REGULAR PAPER

# Phase aberration correction for focused ultrasound transmission by refraction compensation

Japanese Journal of Applied Physics **58**, SGGE22 (2019) **REGULAR PAPER**
https://doi.org/**10.7567/1347-4065/ab19aa**

# Phase aberration correction for focused ultrasound transmission by refraction compensation

Jun Yasuda*, Hideki Yoshikawa*, and Hiroki Tanaka*

*Hitachi. Ltd., Japan*

*E-mail: jun.yasuda.oy@hitachi.com; hideki.yoshikawa.zq@hitachi.com; hiroki.tanaka.wx@hitachi.com

Received November 9, 2018; accepted March 7, 2019; published online July 10, 2019

Phase aberration of focused ultrasound by tissue structure causes focus degradation and reduces the quality of B-mode images. Refraction at the boundary between subcutaneous fat and muscle is one of the dominant factors behind such degradation. To correct this, we propose a refraction compensation method in which ultrasound is transmitted and received twice. The boundary shape between different tissues is detected by the first ultrasound transmission. Next, ultrasound rays from probe elements to the target are calculated taking refraction into account. Corrected delay times are calculated from the length of the rays and the sound velocity of the medium. Finally, ultrasound is transmitted a second time using the corrected delay time and a B-mode image is created. We evaluate the correction effect of the proposed method by numerical simulation and experiments with non-compensated and refraction-compensated cases of intensity distribution of the focused ultrasound. Results show that focus degradation is effectively corrected by the proposed method. 

## 1. Introduction

Medical ultrasound imaging is widely used as a non-invasive and real-time diagnosis technique. Ultrasound images are created by transmitted and received ultrasound using a phased array. Focused ultrasound is extensively used for this purpose. To transmit focused ultrasound, an appropriate delay time is added to the transmission signal of each element. In most ultrasound imaging systems, this delay time is calculated under the assumption that the sound velocity of the medium is homogeneous. However, in real tissue, sound velocity differs according to tissue type. Additionally, in the body, ultrasound is scattered by tissue structure. For this reason, the phase of transmitted ultrasound undergoes aberration and cannot be properly focused. As a result, the shape of the focus is deformed and the ultrasound image is subsequently degraded.[1–10)]

To improve ultrasound images, several methods to correct the phase aberration of transmitted ultrasound have been proposed.[11–27)] The use of iteration has shown great promise in several studies. Reference 25 proposed a method to estimate the appropriate delay time by calculating the correlation of received signals between neighboring elements. Reference 11 reported a method to estimate not only the appropriate delay time but also the amplitude of each element by maximizing the correlation between received and ideal signals from random scatter. Methods using time-reversal have also been studied. Reference 13 proposed a method to estimate the appropriate delay time using time reversal. In this method, ultrasound is transmitted from a focus, and then received by a phased array probe and the arrival time is recorded. Then, the ultrasound is re-emitted by the phased array using an appropriate delay time calculated from the recorded arrival time. Reference 19 reported a method to estimate the appropriate delay time using a time-reversal method for high-intensity focused ultrasound. In this report, the magnetic resonance image of a patient is acquired in advance and a numerical tissue model is created. Then, the time-reversal method is performed by numerical simulation using the numerical tissue model. It was found that the delay time could be calculated accurately by this method, but the disadvantage is that the numerical tissue model must be acquired in advance. Additionally, considering the calculation cost of the procedure, it would be difficult to apply it to real-time diagnosis systems.

On the basis of this background, we propose in this study an efficient method to estimate the delay time in which ultrasound is transmitted and received twice. Ultrasound is first transmitted just to acquire data for detecting the tissue boundary. Next, acoustic rays from the elements on which to focus are calculated taking into account refraction at the tissue boundary. Then, the correct delay time is calculated using the time of flight of each acoustic ray and, finally, the ultrasound is transmitted a second time using the corrected delay time, and an ultrasound image for diagnosis is created. In this method, in order to reduce the calculation cost, we consider only refraction at the tissue boundary: specifically, that between subcutaneous fat and muscle. It makes sense to target refraction because, due to large differences in sound velocity between different tissues, it is one of the dominant factors behind phase aberration. In our method, acoustic rays are assumed to be straight based on ray theory.[28)] However, in a real body, acoustic rays are not completely straight due to inhomogeneous sound velocity and scattering, and this reduces any correction effect. In our previous study,[29)] the correction effect in homogeneous tissue was evaluated using numerical simulation. In this study, we investigate the effect of inhomogeneous sound velocity and scattering. First, we numerically evaluate the correction effect of the proposed method. Specifically, we create a numerical model of homogeneous tissue in order to examine the correction effect under ideal conditions. Next, in an experimental evaluation, we examine the correction effect using real (inhomogeneous) biological tissue. The results of the numerical and experimental evaluations are then compared.

## 2. Material and methods

### 2.1. Principle of refraction compensation

The principle of refraction compensation is outlined in Figs. 1–3. As shown in Fig. 1(a), ultrasound is transmitted from a probe with $N$ elements ($S_1$-$S_N$). The position of the target is $F$. Sound velocities of media 1 and 2 are $c_1$ and $c_2$, respectively. Processing flows of the proposed method are shown in Fig. 2. As shown in (a), ultrasound is transmitted twice. The first transmission is for detecting the boundary

 

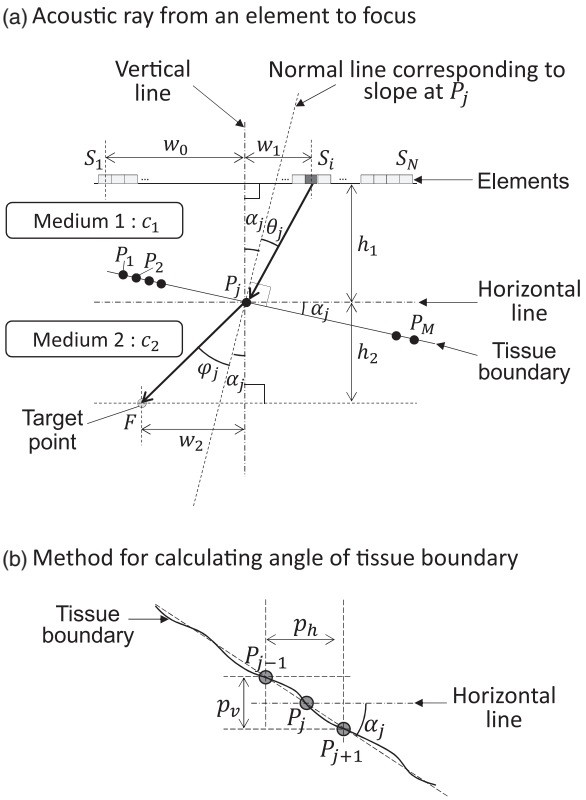


**Fig. 1.** Concept of refraction compensation. (a) Geometrical information for calculating acoustic rays taking into account refraction at a boundary position $P_j$. (b) Method for calculating $\alpha_j$.

shape and the second is for acquiring images with refraction compensation.

The procedure for calculating the delay time is shown in Fig. 2(b). After a boundary shape is detected by the first transmission, the detected boundary is discretized to $M$ points ($P_1$-$P_M$). As shown in Fig. 1(b), the angles of each boundary point $\alpha_j$ are calculated by

$$\alpha_j = \arctan\left(\frac{p_v}{p_h}\right). \tag{1}$$

Next, as shown in Fig. 1, a boundary position $j$ is selected and a ray from $F$ to $P_j$ is defined. Then, $\varphi_j$ is calculated as $\varphi_j = \arctan\left(\frac{w_2}{h_2}\right) - \alpha_j$,(2) and $\theta_j$ is calculated by

$$\theta_j = \arcsin\left(\frac{c_1}{c_2}\sin\varphi_j\right). \tag{3}$$

Equation (3) is derived by Snell's law. By calculating $\theta_j$, a ray from $P_j$ to an element can be defined. Next, element number $i$ is calculated by

$$w_1 = h_1 \tan(\theta_j + \alpha_1), \tag{4}$$

$$i = \frac{w_1 + w_0}{d} + 1, \tag{5}$$

where $d$ is the width of each element. A schematic of the procedure of Eqs. (1)–(5) is provided in Fig. 1.

Then, time of flight (TOF) of $S_i \rightarrow P_j \rightarrow F$ ($t_{\mathrm{TOF}(i)}$) is calculated by

$$t_{\mathrm{TOF}(i)} = \frac{\sqrt{{w_1}^2 + {h_1}^2}}{c_1} + \frac{\sqrt{{w_2}^2 + {h_2}^2}}{c_2}. \tag{6}$$

After calculating all TOF from $S_1$-$S_N$ to $F$, corrected delay times of each element ($t_{\mathrm{Delay}(i)}$) are calculated by

$$t_{\mathrm{Delay}(i)} = \max(T_{\mathrm{TOF}}) - t_{\mathrm{TOF}(i)}, \tag{7}$$

where $T_{\mathrm{TOF}} = \{t_{\mathrm{TOF}(1)}, t_{\mathrm{TOF}(2)}, t_{\mathrm{TOF}(3)}, \cdots t_{\mathrm{TOF}(N)}\}$ and $\max(T_{\mathrm{TOF}})$ indicates the maximum value of $T_{\mathrm{TOF}}$.

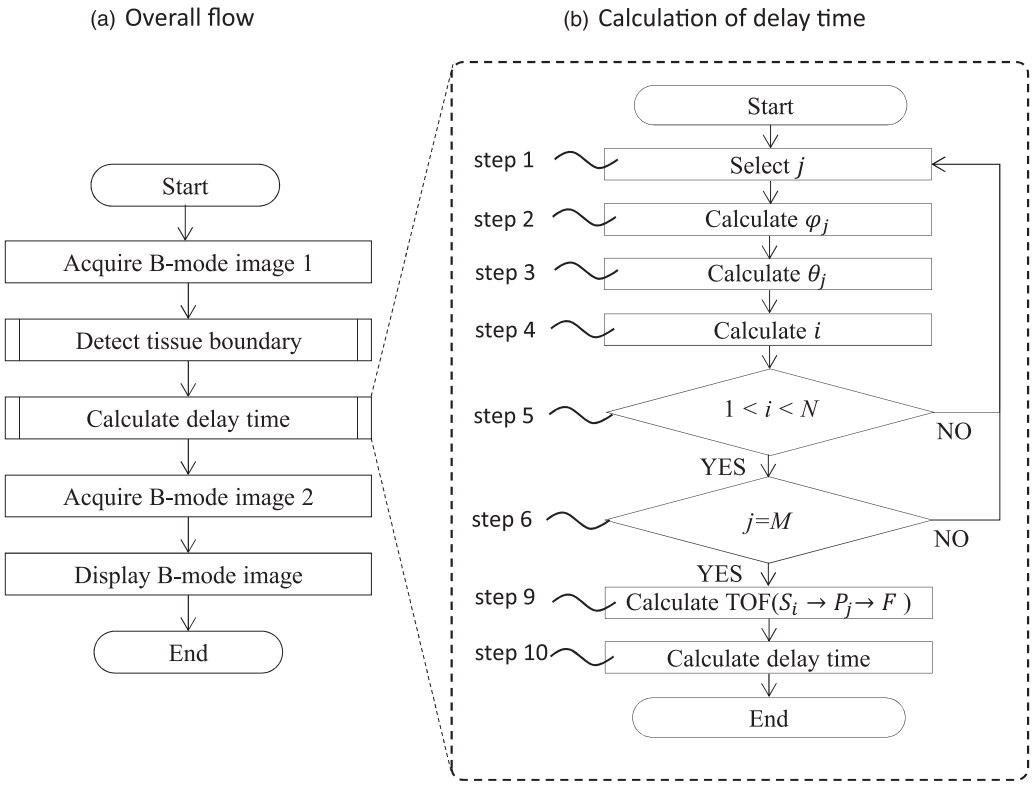


**Fig. 2.** Process flow of refraction compensation. (a) Overall flow. (b) Detailed flow of the delay time calculation.

As indicated in step 5 of Fig. 2(b), if $i < 1$ or $i > N$, return to step 1. In cases where some elements have no rays, the delay times of these elements are interpolated by averaging the delay time of both sides of them. In our method, the sound velocity of each medium is clarified in advance. The B-mode image for boundary detection should be constructed using the sound velocity of fat, as the depth scale in a B-mode image is affected by sound velocity.

Note that Eqs. (5) and (7) can be changed by the relative positions of $S_i$, $P_j$, and $F$. Figure 3 shows acoustic rays in several cases. $S_A$, $S_B$, and $S_C$ indicate the positions of the acoustic source. $F_A$, $F_B$, and $F_C$ indicate the positions of the target. $P$ indicates a point on the tissue boundary. $w_{1A}$, $w_{1B}$, and $w_{1C}$ indicate the horizontal distances between $P$ and $S_A$, $S_B$, and $S_C$, respectively. $w_{2A}$, $w_{2B}$, and $w_{2C}$ also indicate those of $F_A$, $F_B$, and $F_C$, respectively. $h_1$ indicates the vertical distance between $P$ and $S_A$, $S_B$, and $S_C$. $h_2$ indicates the vertical distance between $P$ and $F_A$, $F_B$, and $F_C$. $w_{1A}$-$w_{1C}$ and $w_{2A}$~$w_{2C}$ are expressed by

$$\begin{cases} w_{1A} = h_1 \tan(\theta_A - \alpha_j) \\ w_{1B} = h_1 \tan(\alpha_j - \theta_B), \\ w_{1C} = h_1 \tan(\theta_C + \alpha_j) \end{cases} \tag{8}$$

$$\begin{cases} w_{2A} = h_2 \tan(\varphi_A - \alpha_j) \\ w_{2B} = h_2 \tan(\alpha_j - \varphi_B). \\ w_{2C} = h_2 \tan(\varphi_C + \alpha_j) \end{cases} \tag{9}$$

Equations (2) and (4) can be changed appropriately by considering Eqs. (8) and (9).

Note that our method can be applied even for three tissue layers or more. In the case of three layers, the acoustic path has two refractions, so the method is used twice.

### 2.2. Numerical evaluation of the correction effect

Numerical simulations were performed to evaluate the correction effect of the proposed method. Two-dimensional numerical models were created using the PZFlex simulation software (Fig. 4). Each model had two layers: one consisting of fat and the other of muscle. To evaluate the correction effects under various boundary conditions, we created three types of models with center depths of fat measuring 10, 20, and 30 mm. The boundary between the fat and muscle was created using a photograph of pork. We modeled a linear array probe with an aperture of 15 mm. Focused ultrasound was transmitted from the linear probe. Frequency ultrasound and the number of waves were 5 MHz and 5 cycles, respectively. No apodization was applied. Sound velocity, density, and attenuation coefficient of fat were 1460 m s$^{-1}$, 985 kg m$^{-3}$, and 0.6 dB cm$^{-1}$ MHz$^{-1}$ while those of muscle were 1560 m s$^{-1}$, 1050 kg m$^{-3}$, and 1.2 dB cm$^{-1}$ MHz$^{-1}$. The mesh size lateral and depth directions were 0.15 and 0.30 mm, respectively. The distance from the center of the tissue boundary to ensure an ideal focus was fixed at 40 mm in all three models. In abdomen diagnosis, a physician decides the region of interest (ROI) by considering the depth from the bottom of subcutaneous fat, so the ideal focus depth of each model was 50, 60, and 70 mm. The intensity of spatial peak and temporary peak, $I_{sptp}$, of each point in the measurement ROI was calculated and used to create two-dimensional intensity maps. Lateral intensity profiles of the focus plane, focus plane +5 mm, and focus plane –5 mm were also evaluated. Focus shift and intensity were then quantified on the basis of these profiles.

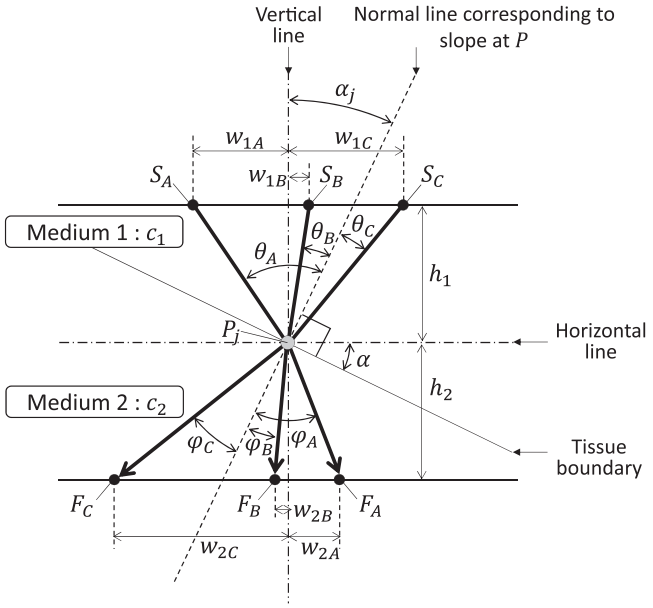


**Fig. 3.** Examples cases of acoustic rays.

### 2.3. Experimental evaluation of the correction effect

The experimental setup of the evaluation system is shown in Fig. 5. A diagnostic ultrasound probe (L75, Hitachi) and a hydrophone (HGL-0085, ONDA) were placed in a water tank filled with 37 °C water. A pork sample containing fat and muscle layers was also set in front of the ultrasound probe. Transmit and receive sequences were controlled flexibly by an ultrasound scanner (Vantage, Verasonics). In this evaluation system, refraction-compensated focused ultrasound was transmitted by the following procedure. First, the Vantage system created a B-mode image of the pork using non-compensated transmission ultrasound. Tissue boundaries on the B-mode image were manually detected by an operator. Next, the corrected delay time was calculated by a refraction compensation method using information on the detected boundary shape. Finally, refraction-compensated ultrasound was transmitted using the corrected delay time. Note that in this experiment, acoustic pressure must be measured in water, so we applied the refraction-compensation method for three layers (fat, muscle, and water). The sound velocity of each medium was measured in advance. Pork fat and muscle were heated at 37 °C, sound velocities were measured at five different positions, and the average sound velocities were used for the evaluation. Measurement results were fat: 1483 m s$^{-1}$, muscle: 1548 m s$^{-1}$, and water: 1523 m s$^{-1}$.

In this experimental evaluation, acoustic intensity distributions of both refraction-compensated and non-compensated focused ultrasound were measured by a hydrophone. The hydrophone was attached to motors and scanned the measurement area automatically. Transmission frequency was 3.5 MHz and the transmission aperture was 15 mm. The focus distance was 50 mm from the probe surface. The measurement areas of the longitudinal and lateral directions were +/– 12 mm and +/– 5 mm from the focus, respectively. Measurement resolution of the longitudinal and lateral directions was 1 mm and 0.25 mm, respectively. The

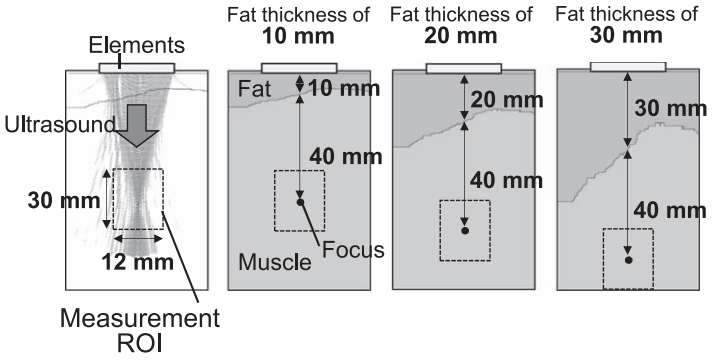


**Fig. 4.** Geometrical information of the numerical models.

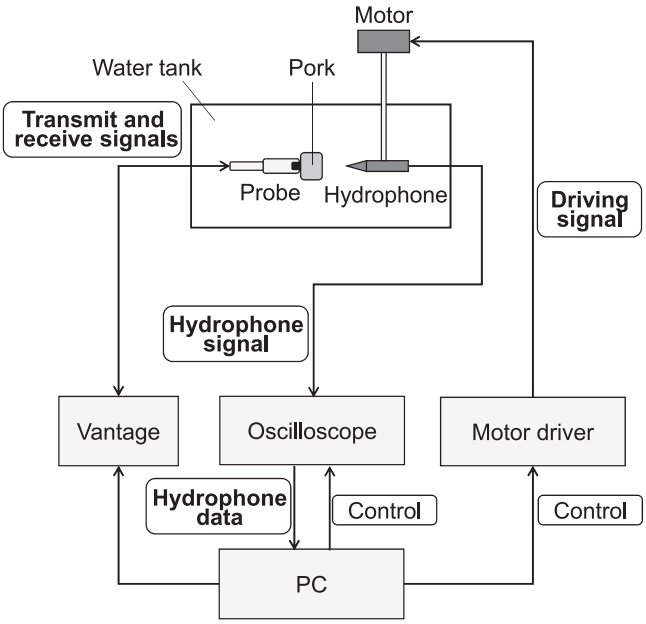


**Fig. 5.** Experimental setup.

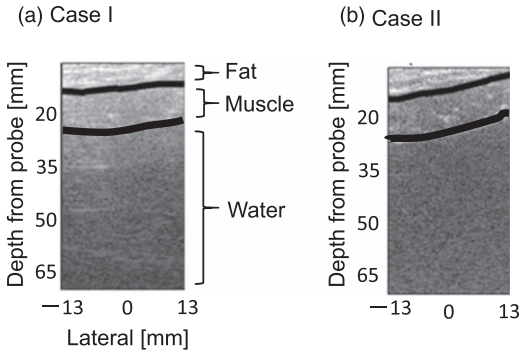


**Fig. 6.** Detected boundary definition.

correction effect was evaluated by comparing the intensity peak position and $I_{sptp}$ between refraction-compensated, non-compensated, and ideal cases. This experiment was performed using two pieces of pork (Case I and Case II) in order to evaluate the different angles of the boundaries. The detected boundaries of each piece are shown in Fig. 6. Black lines indicate the detected boundary. The acoustic pressure distribution in water was also measured as an ideal case (water).

## 3. Results and discussion

### 3.1. Results

**3.1.1. Numerical evaluation.** Figure 7 shows the acoustic intensity distribution around the ideal focus. Ideal focus areas are indicated by white crosses. In the non-compensated cases, the main peak positions were shifted from the target. In the case of 10 and 20 mm, these focuses seemed to shift slightly but not divide. However, in the case of 30 mm, the focus was dramatically divided into two peaks. In contrast, in the compensated cases, the lateral peak positions appeared to be corrected around the target at all fat thicknesses. Additionally, the divided focus at the fat thickness of 30 mm was corrected to a single focus. These results indicate that the refraction compensation method can correct not only shifted focus but also the divided focus.

Lateral intensity profiles of the focus plane, focus +5 mm, and focus –5 mm are provided in Fig. 8, where the horizontal and vertical axes indicate lateral position and intensity, respectively. The target position of the lateral direction is 0 mm. In the non-compensated cases, the peak positions were shifted from the target position at all fat thicknesses. In contrast, in the compensated cases, the peak positions were corrected around the target position. The half widths in the cases of 10, 20, and 30 mm of fat thickness were 0.68, 0.73, and 0.78 mm, respectively. At the fat thickness of 20 and 30 mm, there were side lobes, especially at lateral $> 0$ mm. At the fat thickness of 10 and 20 mm, the half width of the profile on the plane of focus +5 mm was wider than that of the focus and focus –5 mm planes. At the fat thickness of 30 mm, after compensation, the half widths of the profiles were slightly wider than those at 10 and 20 mm.

The quantified peak position on the focus plane is shown in Fig. 9(a). In the non-compensated cases, the focus shift became higher as fat thickness increased. In contrast, in the compensated cases, the peak positions were corrected within 0.15 mm. These corrected positions did not depend on fat thickness. The quantified peak intensity on the focal plane is shown in Fig. 9(b). In both non-compensated and compensated cases, the peak intensity became lower as fat thickness increased. There was no improvement in peak intensity from the proposed method. In the cases of fat thickness of 10 and 20 mm, the intensity of the compensated cases was lower than that of the non-compensated cases.

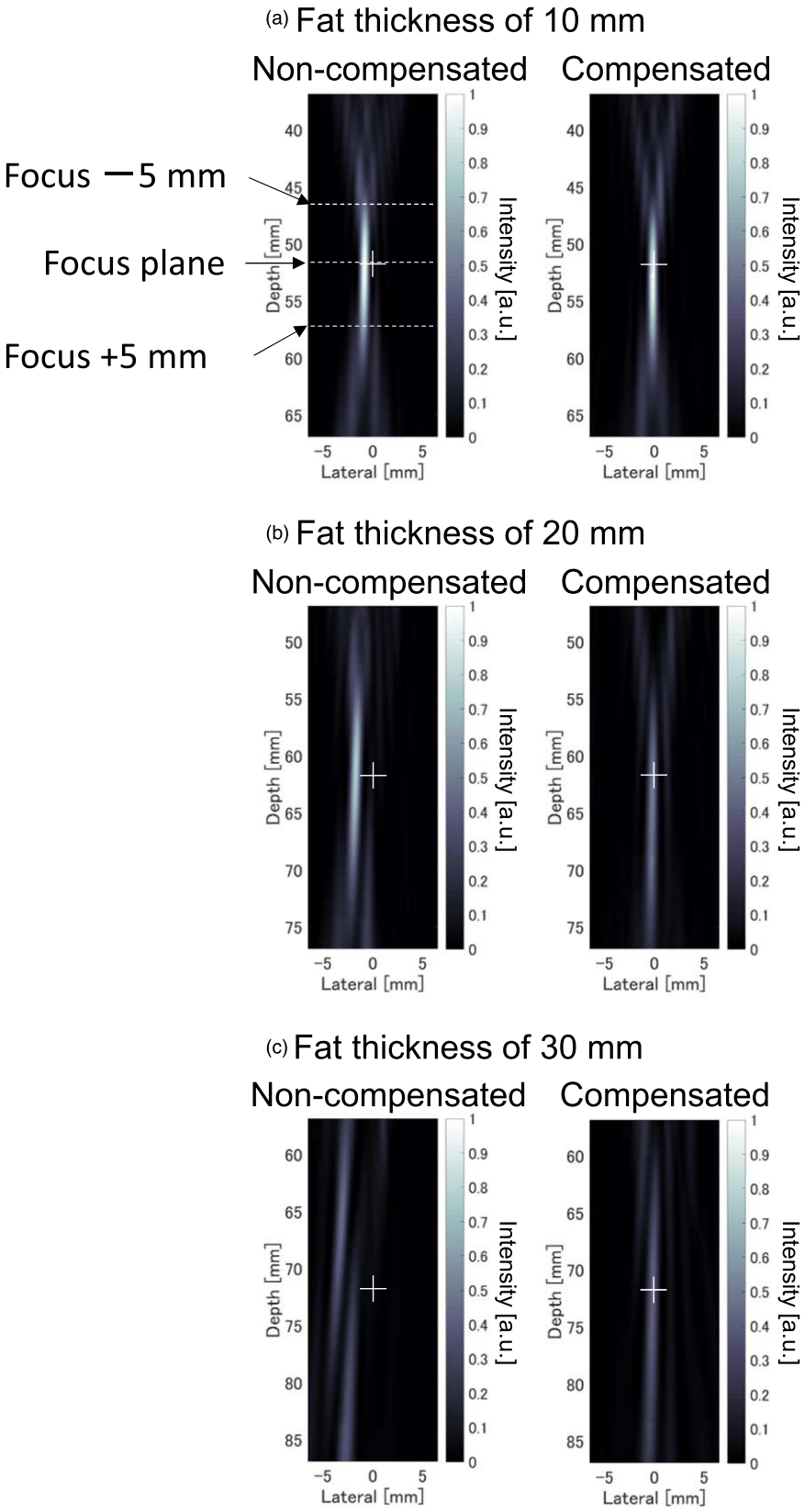


**Fig. 7.** (Color online) Calculated intensity distribution at a fat thickness of (a) 10 mm, (b) 20 mm, and (c) 30 mm.

**3.1.2. Experimental evaluation.** Figure 10–12 show the measured intensity distribution and lateral intensity profiles for water, Case I, and Case II. The ideal focus of each case is indicated by the crossing points of the dotted lines. In Fig. 10, the lateral peak is located at lateral = 0 and the half width of the main lobe is 0.63 mm. In the non-compensated cases, the peak positions were shifted in both Cases I and II, while such shifts were corrected in the compensated cases. In Case II, a side lobe can be seen at lateral $< 0$ mm in both the compensated and non-compensated cases. Table I lists the quantified peak position, intensity, and half width for Cases I and II. In the non-compensated cases, the peak positions were shifted,

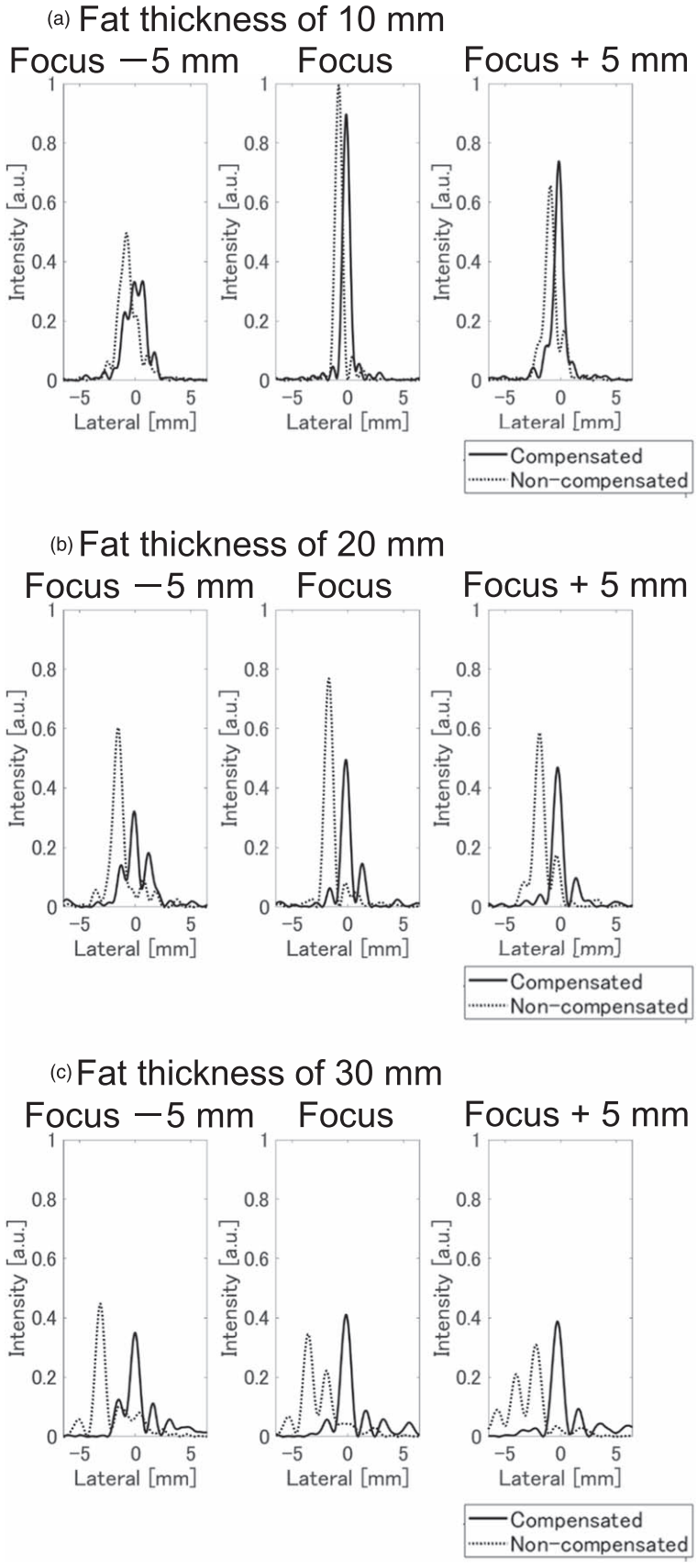


**Fig. 8.** Lateral intensity profiles of each numerical model for fat thickness of (a) 10 mm, (b) 20 mm, and (c) 30 mm.

and the focus shift of Case II was more than twice that of Case I. In the compensated cases, the peak positions of both Cases I and II were corrected to ideal. Interestingly, the peak intensities were not improved in the compensated cases but they were in the non-compensated cases. In Cases I and II, the half widths of the compensated cases were 0.05 and 0.04 mm smaller than those of the non-compensated case, respectively.

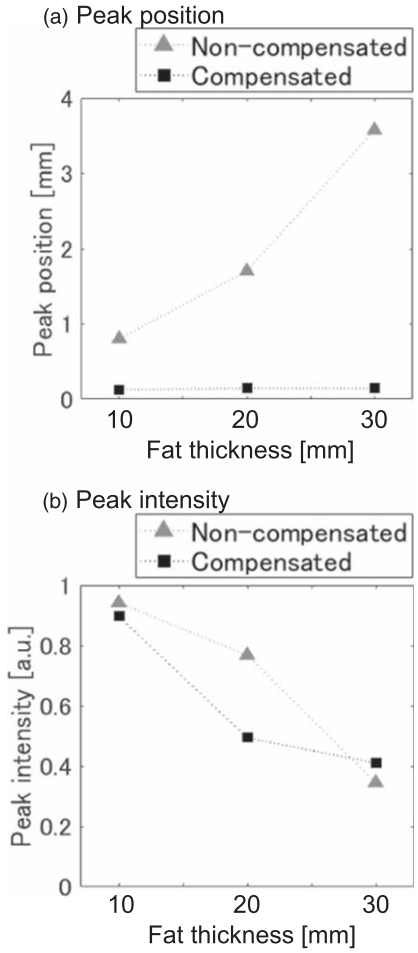


**Fig. 9.** Quantified peak position and peak intensity.

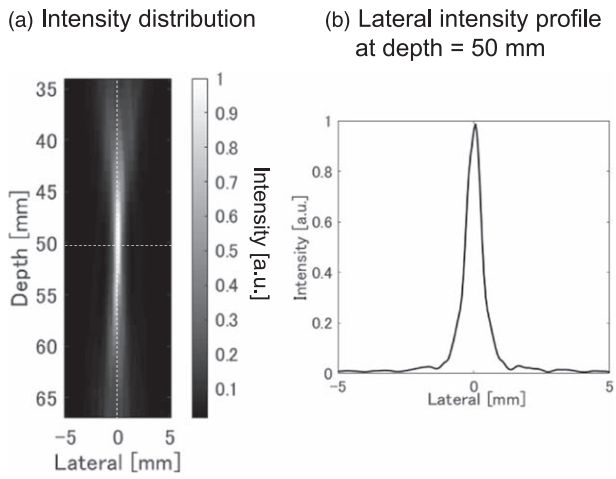


**Fig. 10.** Measurement results for water: (a) intensity distribution around the focus; (b) lateral intensity profile at depth = 50 mm.

**Table I.** Quantified lateral peak positions and intensities of Cases I and II.

| (a) Case I | Non-compensated | Compensated |
|---|---|---|
| Lateral peak position (mm) | −0.500 | 0.00 |
| Peak intensity (a.u.) | 0.852 | 0.816 |
| Half width (mm) | 1.51 | 1.46 |
| (b) Case II | Non-compensated | Compensated |
| Lateral peak position (mm) | −1.25 | 0.00 |
| Peak intensity (a.u.) | 0.692 | 0.614 |
| Half width (mm) | 1.62 | 1.58 |

## 3.2. Discussion

**3.2.1. Numerical evaluation.** In Fig. 9(a), in the non-compensated cases, the lateral peak position was shifted from ideal as fat thickness increased. In the numerical models shown in Fig. 4, the angles of tissue boundary against probe surface increased as fat thickness increased. In the non-compensated cases, the incident angles against the tissue boundary of each acoustic ray, which is indicated as $\theta_j$ in Fig. 1, also increased. Therefore, the effect of refraction on transmitted ultrasound increased, and a larger focus shift occurred. At all fat thicknesses, the lateral peak positions were significantly corrected by refraction compensation, so we conclude that the correction effect for lateral peak position tended to increased as the angles of tissue boundary against the probe surface increased. We had assumed that the shadow and artifact caused by focus shift would be suppressed by refraction compensation but, as shown in Fig. 8, at fat thicknesses of 20 and 30 mm, the side lobes remained even after refraction compensation, and these are what generated the artifact. To reduce the side lobes, we assume the application of apodization would be effective.

In Fig. 9(b), the peak intensity decreased as fat thickness increased. In these numerical models, as fat thickness increased, the acoustic path from the element to the focus became longer. The effect of absorption attenuation increased as the acoustic rays lengthened, and this in turn led to a lower peak intensity. Additionally, peak intensity was not improved by refraction compensation, except at the fat thickness of 30 mm. This is because some refraction-compensated acoustic rays became longer than those that were non-compensated. As mentioned above, absorption attenuation increased as the acoustic rays lengthened, which indicates that refraction compensation does not always improve the peak intensity.

**3.2.2. Experimental evaluation.** From Figs. 11 and 12, we can see that the lateral peak position was corrected by refraction compensation even when real biological tissue was used. As shown in Fig. 6, the angles of the tissue boundary against the probe surface in Case II were bigger than those in Case I. Looking at Figs. 11(b) and 12(b), we can see that the focus shift in Case II was larger than in Case I. This correlation between the angles of tissue boundary and the focus shift is consistent with the results of the numerical simulation. In Case II [Fig. 12(b)], a relatively high-intensity side lobe can be seen in both compensated and non-compensated cases. In contrast, in the case of water [Fig. 10(b)] and Case I [Fig. 11(b)], the intensity of the side lobes was much lower than in Case II. The appearance of side lobes depends on tissue boundary shape, and they cannot be suppressed by refraction compensation. As mentioned in the numerical evaluation, using apodization should be effective to suppress side lobes. In Figs. 11 and 12, we can see that the half width of the main lobe was not changed much by refraction compensation in both Cases I and II. This half width strongly affects the lateral resolution of the B-mode image, so we conclude that lateral resolution was not changed much by refraction compensation. However, the half widths of Cases I and II were wider than that of water. Comparing the numerical and experimental evaluations in terms of biological tissue, we can see that the half widths of the lateral profile were quite different. On the other hand, the

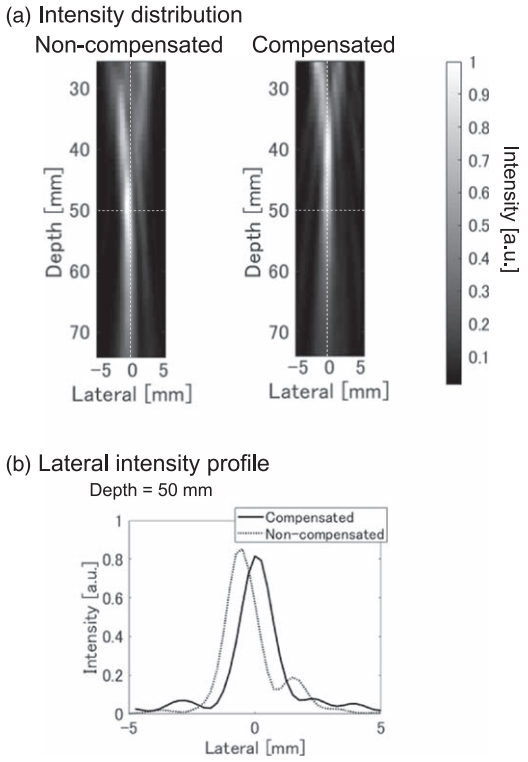


**Fig. 11.** Measurement results for Case I: (a) intensity distribution around the focus; (b) lateral intensity profile at depth = 50 mm.

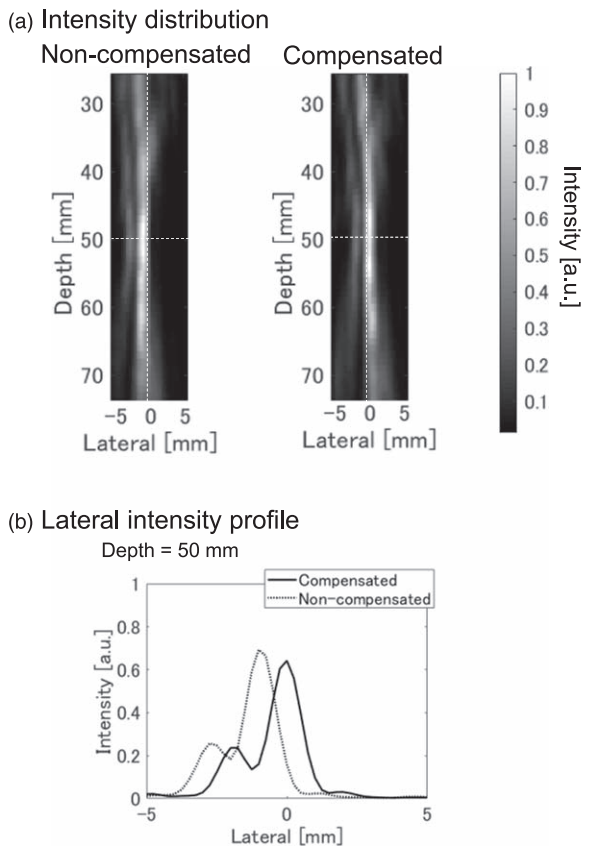


**Fig. 12.** Measurement results for Case II: (a) intensity distribution around the focus; (b) lateral intensity profile at depth = 50 mm.

half widths of the numerical evaluation and experimental evaluation for water were similar. The reason for the difference in half width is the distortion of acoustic rays by inhomogeneous sound velocity and scattering. As mentioned before, the proposed method cannot correct non-straight acoustic rays, so some of these rays did not reach the focus. On the other hand, lateral peak positions were well corrected in both the numerical and experimental evaluations. From this, we conclude that half width and intensity are affected by inhomogeneous sound velocity and scattering. Focus shift, however, is not affected. As mentioned above, in this proposed method, the sound velocity of the media should be clarified in advance. Example methods of sound velocity estimation in clinical practice can be found in Refs. 30, 31, and 32. Of course, the estimation error of sound velocity effects correction effect. Additionally, the correction effect of the focus shift is considered to be further reduced as the distance between the tissue boundary and the focus increases. Further study is required to clarify the improving effect of refraction compensation on B-mode images taking into account inhomogeneous tissue and error in the sound velocity estimation.

## 4. Conclusion

In this study, we proposed refraction compensation to correct the focus degradation of transmission-focused ultrasound. Our method optimizes the delay time of each element of an ultrasound probe taking into account refraction on the tissue boundary. The correction effect was evaluated by both numerical simulation and experiments, and results showed that the lateral focus shift was successfully corrected in both. This focus shift correction is expected to suppress shadow and artifacts in B-mode images. As future work, we will clarify the improving effect of refraction compensation on B-mode images taking into account inhomogeneous tissue and error in the sound velocity estimation.

1) T. D. Mast, L. M. Hinkelman, and M. J. Orr, J. Acoust. Soc. Am. **102**, 1177 (1997).
2) L. M. Hinkelman, T. D. Mast, L. A. Matlay, and R. C. Waag, J. Acoust. Soc. Am. **104**, 3635 (1998).
3) L. M. Hinkelman, T. D. Mast, L. A. Matlay, and R. C. Waag, J. Acoust. Soc. Am. **104**, 3651 (1998).
4) M. Tabei, T. D. Mast, and R. C. Waag, J. Acoust. Soc. Am. **113**, 1166 (2003).
5) T. Varslot, H. Krogstad, E. Mo, and B. A. Angelsen, J. Acoust. Soc. Am. **115**, 3068 (2004).
6) M. V. Aarssen, M. A. Verhoef, and J. M. Thijssen, J. Acoust. Soc. Am. **85**, 567 (1989).
7) T. D. Mast, L. M. Hinkelman, L. A. Metlay, M. J. Orr, and R. C. Waag, J. Acoust. Soc. Am. **106**, 3665 (1999).
8) M. O'Donnell and S. W. Flax, IEEE. Trans. Ultrason. Ferro and Freq. Contl. **35**, 768 (1988).
9) K. Matsui, T. Azuma, K. Fujiwara, H. Takeuchi, K. Itani, J. Wang, T. Iwahashi, E. Kobayashi, and I. Sakuma, Jpn. J. Appl. Phys. **56**, 057301 (2017).
10) Y. Kobayashi, T. Azuma, K. Shimizu, M. Koizumi, T. Oya, R. Suzuki, K. Maruyama, K. Seki, and S. Takagi, Jpn. J. Appl. Phys. **57**, 07LF22 (2018).
11) S.-E. Måsøy, T. F. Jphansen, and B. Angelsen, J. Acoust. Soc. Am. **113**, 2009 (2003).
12) S.-E. Måsøy, T. F. Jphansen, and B. Angelsen, J. Acoust. Soc. Am. **117**, 450 (2005).
13) M. Fink, IEEE. Trans. Ultrason. Ferro and Freq. Contl. **39**, 555 (1992).
14) G. Montaldo, M. Tanter, and M. Fink, J. Acoust. Soc. Am. **115**, 768 (2004).
15) J.-L. Robert and M. Fink, J. Acoust. Soc. Am. **124**, 3659 (2008).
16) W. Olbricht, M. Sistla, G. Ghandi, G. Lewis, and A. Sarvazyan, J. Acoust. Soc. Am. **134**, 1569 (2013).

17) N. Quieffin, S. Catheline, R. K. Ing, and M. Fink, J. Acoust. Soc. Am. **115**, 1955 (2004).
18) E. G. Asgedom, L.-J. Gelius, A. Austeng, S. Holn, and M. Tygel, J. Acoust. Soc. Am. **130**, 2024 (2011).
19) R. Narumi, K. Matsuki, S. Mitarai, T. Azuma, K. Okita, A. Sasaki, K. Yoshinaka, S. Takagi, and Y. Matsumoto, Jpn. J. Appl. Phys. **52**, 07HF01 (2013).
20) H. Taki and T. Sato, Jpn. J. Appl. Phys. **49**, 07HF08 (2010).
21) J. C. Tilettm, J. P. Astheimer, and R. C. Waag, IEEE. Trans. Ultrason. Ferro and Freq. Contl. **57**, 214 (2010).
22) D. Liu and R. C. Waag, J. Acoust. Soc. Am. **96**, 649 (1994).
23) D. Li, G. Shen, J. Bai, and Y. Chen, IEEE Trans. Biomed. Eng. **58**, 1621 (2011).
24) L. Nock and G. E. Trahey, J. Acoust. Soc. Am. **85**, 1819 (1989).
25) S. W. Flax and M. O'Donnell, EEE. Trans. Ultrason. Ferro and Freq. Contl. **35**, 758 (1988).
26) C. Dorme and M. A. Fink, IEEE. Trans. Ultrason. Ferro and Freq. Contl. **43**, 167 (1996).
27) L. A. F. Ledoux and A. P. Berkhoff, IEEE. Trans. Ultrason. Ferro and Freq. Contl. **43**, 158 (1996).
28) A. A. Hudimac, J. Acoust. Soc. Am. **29**, 916 (1957).
29) J. Yasuda, Proc. The 39th Symp. on UltraSonic Electronics, 2018 2P5-2.
30) J. F. Krucker, J. B. Fowlkes, and P. L. Carson, IEEE. Trans. Ultrason. Ferro and Freq. Contl. **51**, 1095 (2004).
31) M. H. Cho, L. H. Kang, J. S. Kim, and S. Y. Lee, Ultrasonics **49**, 774 (2009).
32) H. Hachiya, S. Ohtsuki, M. Tanaka, and F. Dann, J. Acoust. Soc. Am. **92**, 1564 (1992).